

Dynamical Characteristics of Quasi-6-day Rossby Waves and Gravity Waves during the Stratospheric Sudden Warming in the Southern Hemisphere in 2019

Yuichi Minamihara¹, Kaoru Sato¹, and Shingo Watanabe²

¹University of Tokyo

²Japan Agency for Marine-Earth Science and Technology

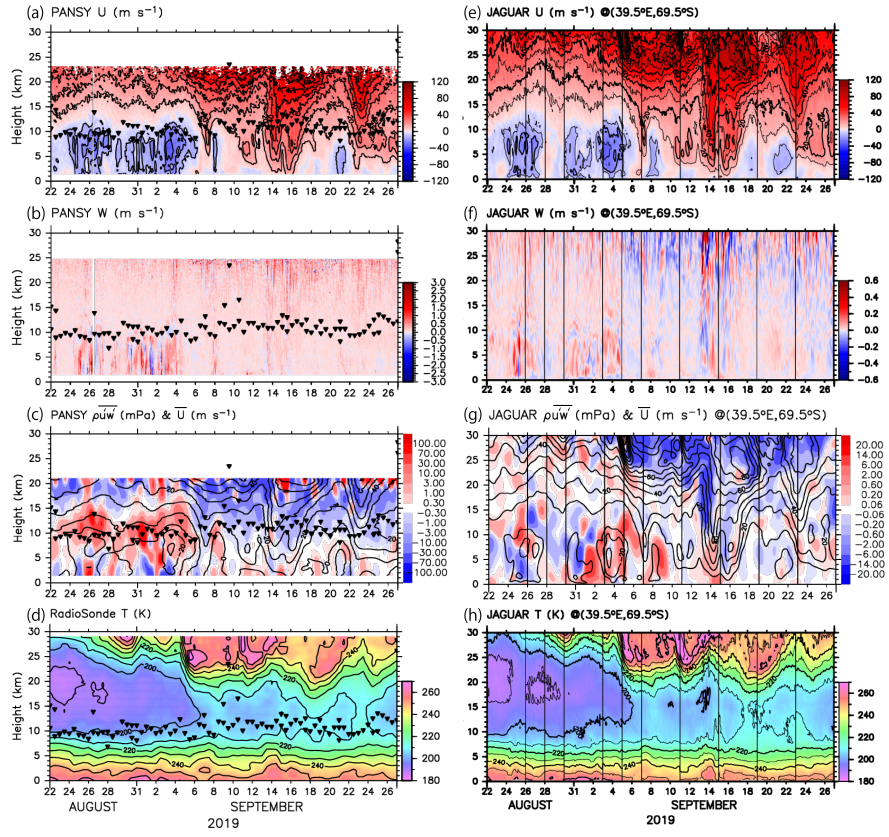
November 24, 2022

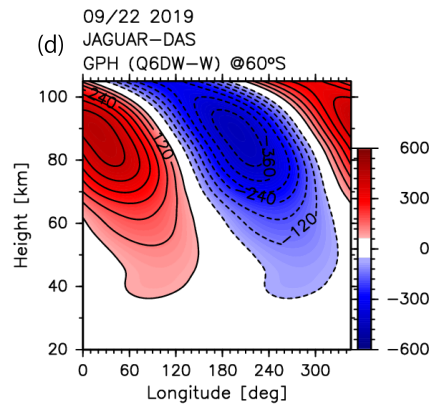
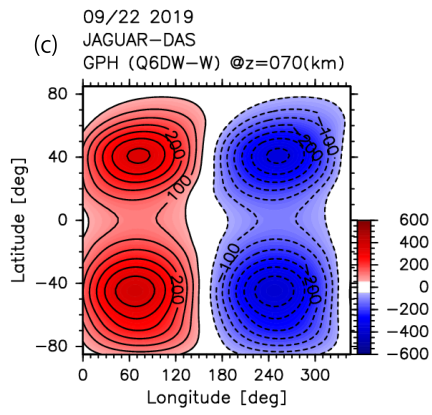
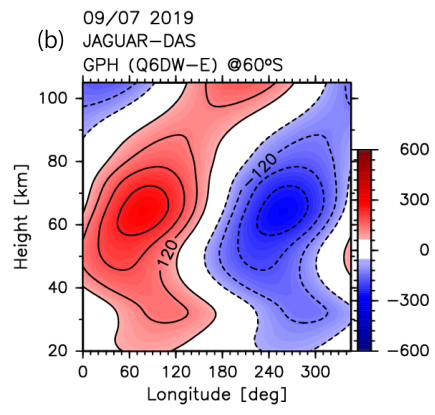
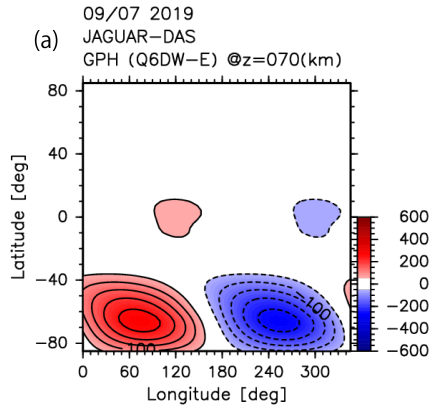
Abstract

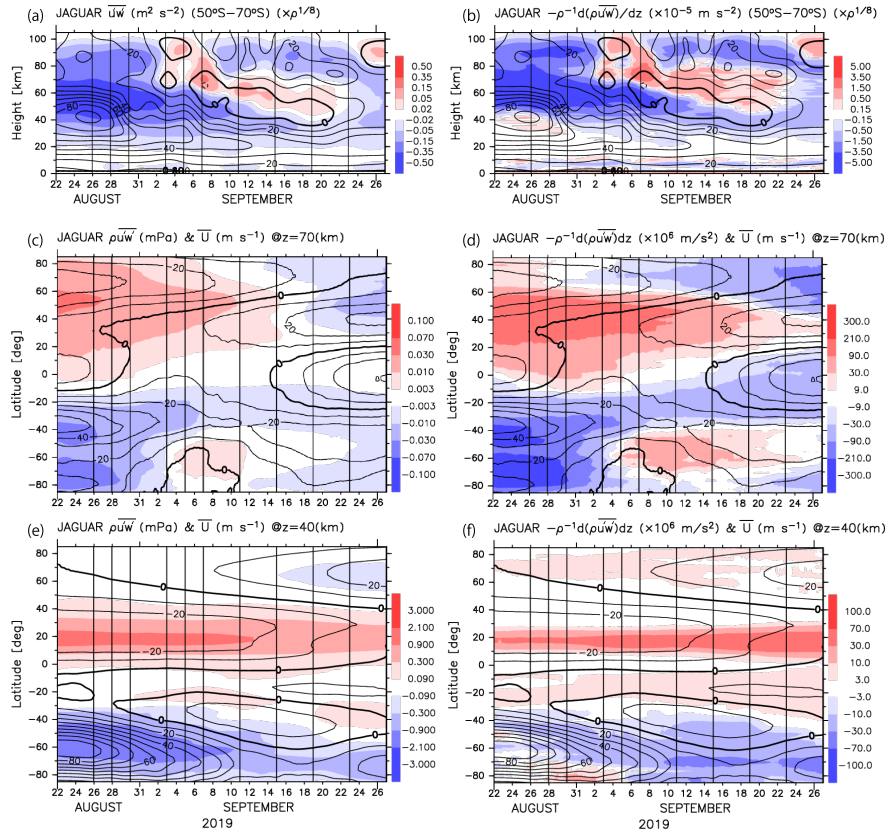
In September 2019, a minor but strong sudden stratospheric warming (SSW) event occurred in the Southern Hemisphere. We examine the dynamical characteristics of the gravity waves (GWs) and Rossby waves (RWs), especially quasi-6-day waves (Q6DWs), during this event based on Program of the Antarctic Syowa (PANSY) radar observations and high-resolution Japanese Atmospheric General circulation model for Upper Atmosphere Research (JAGUAR) simulations. For the GWs, strongly negative vertical fluxes of zonal momentum in the stratosphere were observed around the edge of the polar vortex during the SSW event. In the mesosphere, strongly positive momentum fluxes were observed in the Eastern Hemisphere, where westward winds were dominant associated with the SSW event. For the RWs, two types of Q6DWs appeared during the SSW event: one with eastward phase velocity (Q6DW-E) and one with westward phase velocity (Q6DW-W). These waves had a baroclinic structure in vertical, differing from normal-mode 5-day Rossby waves. It is shown that Q6DW-E, which was observed prior to the SSW onset, was an unstable wave owing to the baroclinic instability in the high-latitude mesosphere. Conversely, Q6DW-W was observed after the onset and had characteristics of an upward-propagating internal RW. It is considered to be generated by barotropic/baroclinic instability in the upper stratosphere. This instability was likely caused by forcings resulting from the in situ generated Q6DW-E and RWs originating from the mid- and high-latitude troposphere, as well as the GW forcings, which were positive in the mesosphere and negative in the stratosphere associated with the SSW event.

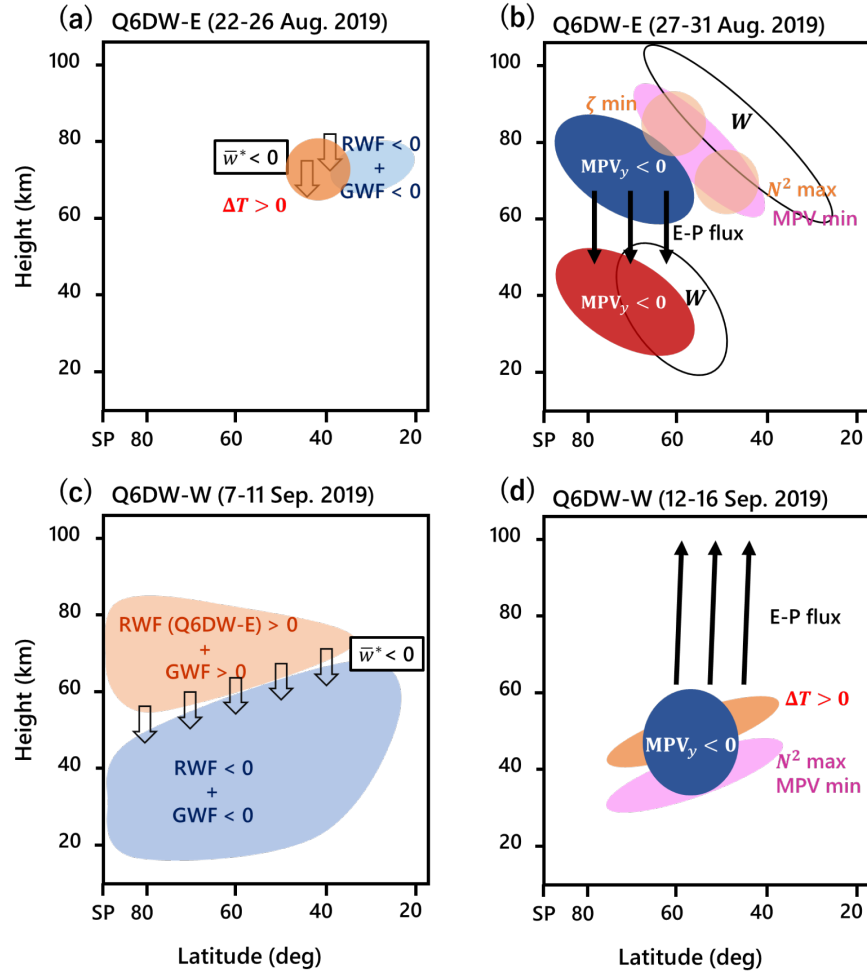
Hosted file

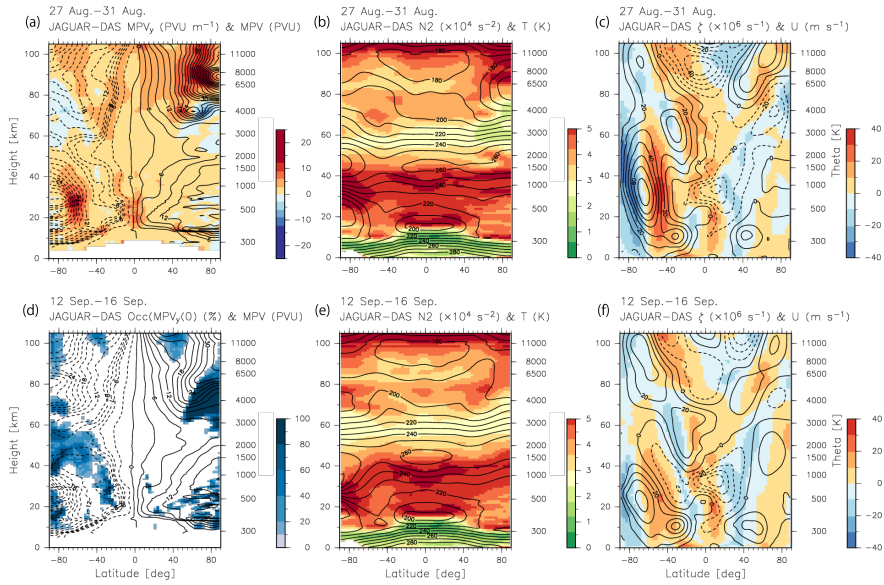
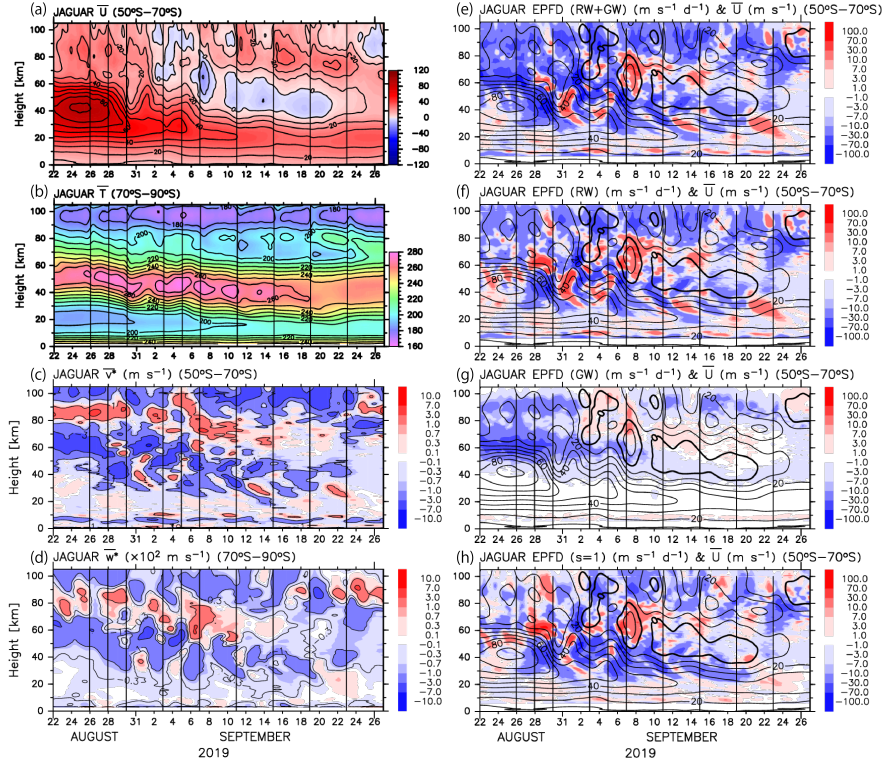
essoar.10511060.1.docx available at <https://authorea.com/users/553206/articles/605042-dynamical-characteristics-of-quasi-6-day-rossby-waves-and-gravity-waves-during-the-stratospheric-sudden-warming-in-the-southern-hemisphere-in-2019>











Yuichi Minamihara¹, Kaoru Sato¹, and Shingo Watanabe²

¹Department of Earth and Planetary Science, Graduate School of Science, The University of Tokyo, Tokyo, Japan

²Japan Agency for Marine-Earth Science and Technology (JAMSTEC), Yokohama, Japan

Corresponding author: Yuichi Minamihara (minamihara@eps.s.u-tokyo.ac.jp)

Key Points:

- Westward forcing by gravity waves was observed in the westward wind region of the mesosphere during the SSW in the Southern Hemisphere
- A quasi-6-day wave (Q6DW) with zonal wavenumber one consists of two Rossby waves with eastward and westward phase velocities, respectively
- The eastward-propagating Q6DW was an unstable wave generated by the baroclinic instability and, along with the westward gravity wave forcing, was responsible for the generation of the westward-propagating Q6DW

Abstract

In September 2019, a minor but strong sudden stratospheric warming (SSW) event occurred in the Southern Hemisphere. We examine the dynamical characteristics of the gravity waves (GWs) and Rossby waves (RWs), especially quasi-6-day waves (Q6DWs), during this event based on Program of the Antarctic Syowa (PANSY) radar observations and high-resolution Japanese Atmospheric General circulation model for Upper Atmosphere Research (JAGUAR) simulations. For the GWs, strongly negative vertical fluxes of zonal momentum in the stratosphere were observed around the edge of the polar vortex during the SSW event. In the mesosphere, strongly positive momentum fluxes were observed in the Eastern Hemisphere, where westward winds were dominant associated with the SSW event. For the RWs, two types of Q6DWs appeared during the SSW event: one with eastward phase velocity (Q6DW-E) and one with westward phase velocity (Q6DW-W). These waves had a baroclinic structure in vertical, differing from normal-mode 5-day Rossby waves. It is shown that Q6DW-E, which was observed prior to the SSW onset, was an unstable wave owing to the baroclinic instability in the high-latitude mesosphere. Conversely, Q6DW-W was observed after the onset and had characteristics of an upward-propagating internal RW. It is considered to be generated by barotropic/baroclinic instability in the upper stratosphere. This instability was likely caused by forcings resulting from the in situ generated Q6DW-E and RWs originating from the mid- and high-latitude troposphere, as well as the GW forcings, which were positive in the mesosphere and negative in the stratosphere associated with the SSW event.

1 Introduction

Sudden stratospheric warming (SSW) events significantly modify the thermal

and dynamical conditions in the winter stratosphere. They occur as a result of interactions between upward-propagating Rossby waves (RWs) from the troposphere and the zonal-mean zonal winds (Matsuno, 1971). SSW events play a major role in the stratosphere with respect to Arctic and Antarctic ozone variability (e.g., Schoeberl & Hartmann, 1991) and material transport and chemistry (e.g., Manney et al., 2009). SSW events can also influence the troposphere with respect to decadal variability in the North Atlantic Ocean circulation (e.g., Reichler et al., 2012), equatorial convective activity (e.g., Kodera, 2006), and high-latitude cloud amounts (Kohma & Sato, 2014).

In September 2019, a strong SSW in the Southern Hemisphere occurred (Rao et al., 2019). During this event, which is hereafter referred to as SSW-SH 2019, the zonal-mean zonal winds at 10 hPa and 60° S did not fully reverse, hence the conditions for a major SSW were not met (Butler et al., 2015). However, the magnitude of the temperature increase during early spring was comparable to that in 2002, which is currently the only previously observed major warming event in the Southern Hemisphere (Lim et al., 2020). The SSW-SH 2019 event started when the polar vortex was quite strong and cold. Conversely, the 2002 event occurred in late September and involved a vortex that was more favorably pre-conditioned for warming.

Several previous studies general circulation models (GCMs) have focused on the roles of RWs and gravity waves (GWs) during SSW events. Tomikawa et al. (2012) examined a major SSW event that occurred spontaneously in a free-run simulation over three model years using a GW-permitting high-resolution GCM developed by the Kanto project with the model top at a height of $z = 85$ km (Watanabe et al., 2008). They showed that a positive RW forcing, which corresponds to an eastward acceleration of the zonal-mean zonal wind, leads to a quick recovery of the polar night jet after a major SSW event. Negative GW forcing, corresponding to a westward acceleration of the zonal-mean zonal wind, above the recovering westerly jet contributes to the elevated stratopause (ES) formation at $z = \sim 75$ km.

Limpasuvan et al. (2016) examined the responses in the mesosphere and lower thermosphere (MLT) region to SSW events simulated using the Whole Atmosphere Community Climate Model, Version 4 with specified dynamics (SD-WACCM) for the period of 1990–2013. They showed that the filtering effect of the weakened stratospheric jet allows eastward-propagating GWs to penetrate the winter MLT region. The GWs provide positive forcing, which causes winter polar mesospheric cooling. The polar mesospheric westerly jet is reformed at higher altitudes via a combination of the GW forcing and radiative relaxation. Then, the negative GW forcing reappears in the upper part of the polar jet, causing a stronger downwelling near the pole, and helps formation of the stratopause at an elevated altitude.

In addition, simple vertical propagation of GWs and RWs from the troposphere is insufficient to explain the momentum budget in the middle atmosphere. The in situ generation of waves in the middle atmosphere therefore needs to be con-

sidered. Sato and Nomoto (2015) indicated the importance of the interplay of GWs and RWs in the middle atmosphere. Using the Kanto model outputs, they showed that in situ RW generation occurs as a result of the barotropic and/or baroclinic instability (hereafter referred to as dynamical instability). This dynamical instability is associated with a potential vorticity maximum at mid-latitudes caused by the forcing of GWs originating from the troposphere. Two types of RWs, propagating eastward and westward, are generated and cause positive and negative forcing, respectively, eliminating the potential vorticity maximum. Watanabe et al. (2009) also examined the generation mechanism of eastward 4-day waves in the winter mesosphere in the Southern Hemisphere caused by dynamical instabilities. Such in situ generation of waves and the forcing of the waves via their dissipation in remote regions significantly contribute to the momentum budget in the MLT region (Sato et al., 2018; Yasui et al., 2018, 2021).

Okui et al. (2021) examined the formation mechanism of the ES and the mesospheric inversion layer (MIL) during the SSW event, using outputs from a hindcast of a major SSW event with an ES in 2018/2019 using a GW-permitting high-resolution GCM called the Japanese Atmospheric General circulation model for Upper Atmosphere Research (JAGUAR) (Watanabe & Miyahara, 2009). They showed that the negative RW forcing generated by the dynamical instability in the middle atmosphere contributes to MIL formation. The GW forcing helps dynamical instability formation. They also noted that both GW and RW forcings above the recovered westerly jet play crucial roles in ES formation.

Yamazaki et al. (2020) reported that the quasi-6-day wave (Q6DW) was enhanced in the lower-latitude ionosphere during SSW-SH 2019. Strong quasi-6-day oscillations were observed in ionospheric parameters such as the equatorial electron jet and the electron density. The quasi-6-day variation in the equatorial electron jet has a westward-moving structure with zonal wavenumber 1. The dynamical characteristics of Q6DWs, however, are still not fully understood. Several studies have proposed different excitation mechanisms for Q6DWs, including Doppler-shifted 5-day normal-mode RWs (Wu et al., 1994), RWs excited and/or amplified by dynamical instabilities in the middle atmosphere (Lieberman et al., 2003; Liu et al., 2004; Meyer & Forbes, 1997), and internally forced waves having a coherent phase structure from the troposphere to the mesopause (Talaat et al., 2002). Normal-mode 5-day RWs have a nearly barotropic structure in the stratosphere and an equatorially symmetric geopotential height (GPH) perturbation with an amplitude maximum near latitudes of 40° (e.g., Hirota et al., 1983).

The aim of this study is to examine the dynamical characteristics of GWs and RWs, including Q6DWs, from the surface to the MLT region during SSW-SH 2019 using hindcast data generated by JAGUAR and observational data from the Program of the Antarctic Syowa (PANSY) radar and radiosondes at Syowa Station in the Antarctic. A detailed description of the observations and numerical simulations is given in Section 2. In Section 3, we present the time evolution

of the distribution of the GWs from the stratosphere to the MLT region. The dynamical characteristics and excitation mechanisms of Q6DWs during SSW-SH 2019 are examined in Section 4. A summary and concluding remarks are given in Section 5.

2 Data Description and Methodology

2.1 PANSY Radar observations

The PANSY radar is the first Mesosphere-Stratosphere-Troposphere/Incoherent Scatter radar (Sato et al., 2014) that was installed at Syowa Station in the Antarctic (69.0°S, 39.6°E) in early 2011. This radar is a monostatic pulse VHF Doppler radar with a central frequency of 47 MHz in which an active phased array system consisting of 1,045 crossed-Yagi antennas is employed.

During SSW-SH 2019, the PANSY radar was continuously operated, interleaving the troposphere/stratosphere observation mode and the mesosphere observation mode. The time resolution of each observation mode was ~ 90 s. In the troposphere/stratosphere observation, five beams, i.e., a vertical beam and four oblique beams tilted to the east, west, north, and south with a zenith angle of 10° , were used. Line-of-sight velocities from each beam were obtained with a range interval (Δr) of 150 m. The observation time interval (Δt) was approximately 220 s, including the time required for switching the two observation modes. The accuracy of the line-of-sight velocity was ~ 0.1 m s^{-1} . We did not use the mesosphere observation mode data because it was sparse in time during the winter as a result of the weak ionization in the mesosphere associated with the weak solar radiation. The zonal, meridional, and vertical winds and vertical fluxes of the zonal and meridional momentum estimated from the line-of-sight velocities in the five directions were analyzed in this study. For details concerning the estimation method for the three-dimensional winds and momentum fluxes, see Section 2.1 of Minamihara et al. (2020).

Additional fittings were performed for the radar echo spectra, which were integrated every 30 min. This method effectively reduced the statistical noise and allowed an estimation of the three-dimensional winds at higher altitude ranges compensating for the lower temporal resolution (Sato et al., 1997). Following Minamihara et al. (2018), we defined the GW components (represented by a prime) as the wave components with periods shorter than 1 day and with vertical wavelengths of 5 km or less.

Figure 1a and 1b shows time-height sections of the zonal (u) and vertical winds (w) from the PANSY radar observations, respectively. Before 4 September 2019, westward winds with a maximum of ~ 30 m s^{-1} over the entire troposphere and relatively weak eastward winds with a maximum of ~ 40 m s^{-1} in the lower stratosphere are observed. Moreover, in the troposphere, strong vertical wind disturbances with amplitudes greater than 1 m s^{-1} are observed. Conversely, after 4 September, eastward winds are dominant not only in the lower stratosphere but also in the troposphere. The eastward winds in the stratosphere become stronger with values of up to ~ 80 m s^{-1} . Strong vertical wind disturbances are

observed in the height region of $z > 18$ km in the stratosphere, whereas those in the troposphere are weaker. Figure 1c shows a time-height section of the vertical fluxes of the zonal momentum ($\overline{u'w'}$). The overbar indicates the 1-day running mean. Before 4 September, relatively largely positive $\overline{u'w'}$ in the height region of $z < 15$ km and weakly negative $\overline{u'w'}$ in the height region of $z > 15$ km are observed. After 4 September, negative $\overline{u'w'}$ is dominant in the upper troposphere and lower stratosphere. Especially around 13 September, the magnitude of $\overline{u'w'}$ is large in the height region of $z > 15$ km.

2.2 Radiosonde Observations

At Syowa Station, operational radiosonde observations are made twice a day. From 26 August 2019 to 2 October 2019, additional radiosonde observations targeting SSW-SH 2019 were performed once or twice a day. The ascending speed of the radiosondes was adjusted to 5–6 m s⁻¹. The temperature (T), humidity, horizontal winds, and pressure were obtained every second. For the operational observations, a balloon was launched at 23:30 UTC and 11:30 UTC. For the additional observations, a balloon was launched at 0530 UTC and/or 1730 UTC. Sixty-five observations were successfully performed.

Figure 1d shows the time-height section of T observed by the radiosondes. Note that the radiosonde observations provide T and the horizontal winds in height regions lower than 1.5 km where PANSY radar observations are not available. A sharp increase in T is observed in the height region of $z > 25$ km during the periods of 28–31 August and 2–4 September. Furthermore, the increase in T is significant in the height region of $z > 22$ km during the periods of 5–8, 11–13, 18–21, and 24–26 September. These time periods correspond well to periods when strong eastward winds are observed in the lower stratosphere in Figure 1a.

2.3 JAGUAR Simulations

Numerical simulations using JAGUAR were performed to examine the dynamical characteristics of the RWs and GWs from the surface to the MLT region during SSW-SH 2019. The model setup in this study is the same as that of Okui et al. (2021). The model had 340 vertical layers (L340) from the surface to GPH of ~150 km, with a log-pressure height interval of ~300 m in the middle atmosphere. The triangularly truncated spectral resolution was T639, corresponding to a minimum resolvable horizontal wavelength of ~60 km. Therefore, the model can resolve a major part of the GWs. The longitudinal and latitudinal intervals of the model outputs were 0.1875°. No parameterizations for the GWs were used.

As initial values in the JAGUAR simulations, we used data from the JAGUAR-Data Assimilation System (JAGUAR-DAS) (Koshin et al., 2020, 2021). This system assimilated the PREPBUFR observational data set, temperature data from the Aura Microwave Limb Sounder (MLS) and the Sounding of the Atmosphere using Broadband Emission Radiometry (SABER), and radiation

data from the Special Sensor Microwave Imager/Sounder (SSMIS) via the four-dimensional local ensemble transform Kalman filter (4D-LET-KF) using a medium-resolution (T42L124) version of JAGUAR.

The time period of the high-resolution JAGUAR simulations is 36 days, from 22 August 2019 to 26 September 2019. This was divided into consecutive 4-day periods and an independent model run was performed for each 4-day period. Each model run consisted of a 3-day spectral nudging for low wavenumber smaller than 42 and a 4-day free run. We analyzed only the output data from the 4-day free runs. This method reduces discrepancies from the real atmosphere and allows the model to freely simulate GWs, even though discontinuities appear between the runs. When the Courant-Friedrichs-Lewy condition was not satisfied because of a strong jet (26-29 August and 3-6 September), we shortened the time period of the free runs from 4 days to 2 days. In total, 11 simulations were performed such that the free-run outputs continuously filled the entire 36-day period. The black thin lines in Figures 1e–1h show the time period of the free run in each simulation.

In the analysis of the momentum budget, the disturbances were divided into RW and GW components as follows. First, the diurnal migrating tide having a zonal wavenumber (s) of 1 and the semi-diurnal migrating tide with $s = 2$ were extracted from the original data. Next, the remaining components with $s = 1$ –20 were designated as RWs and the components with a total wavenumber (n) of more than 20 ($n \geq 21$) were designated as GWs. Especially for the comparisons with the PANSY radar observations, we focused on the GW components having a wave period of less than 1 day.

Figures 1e, 1f, 1g, and 1h show the time-height sections of u , w , $\overline{u'w'}$ and T , respectively, from the high-resolution JAGUAR simulations at (39.0°E, 69.0°S), which is the nearest grid point to Syowa Station. For u , not only large-scale structures but also wave-like structures having a wave period of ~ 12 h in the lower stratosphere, as observed by the PANSY radar, are well reproduced. Furthermore, the enhancement of the eastward wind and T in the height region of $z > 22$ km are consistent with the observations. For w , JAGUAR reproduces intermittent and strong disturbances, such as the disturbance penetrating from the ground to the lower stratosphere during the period of 12–14 September. The region with $\overline{u'w'} < 0$ in the lower stratosphere is well reproduced after 4 September, while the sign of $\overline{u'w'}$ in the troposphere is not necessarily consistent with the PANSY radar observations (Figure 1c) before 4 September. The magnitude of the vertical wind disturbances and $\overline{u'w'}$ values simulated by JAGUAR, however, are approximately $\frac{1}{4}$ – $\frac{1}{5}$ of those from the PANSY radar observations.

The comparison between the radar observations and the model simulations confirms that JAGUAR can reproduce not only the large-scale u and T behavior but also the distribution and intermittent features of GWs above Syowa Station, even though the magnitude of the GW momentum fluxes was somewhat underestimated by JAGUAR. It has been reported that vertical wind disturbances

associated with orographic GWs (Minamihara et al., 2018) and/or hydraulic jumps (Tomikawa et al., 2015) are frequently observed over the Syowa Station. In addition to the insufficient model resolution, the lack of an adequate reproduction of the steep terrain structure in the JAGUAR simulations may also be major reason for the weak vertical wind disturbance. Note that the magnitude of the GW forcings seen in the momentum budget during SSW-SH 2019 could be up to five times larger in the real atmosphere.

Next, we focus on the dynamical characteristics of SSW-SH 2019. Figures 2a–d show time-height sections of the zonal-mean zonal wind (\bar{U}), zonal-mean temperature (\bar{T}), and the meridional (\bar{v}^*) and vertical (\bar{w}^*) components of the residual mean circulation, respectively. Figures 2e–h show time-height sections of the wave forcings associated with all of the wave components, RWs, GWs, and the $s = 1$ RW, respectively.

A high-temperature region descent from $z = 40$ – 60 km by ~ 10 km is observed three times during late August and early September, namely, on 30 August, 3 September, and 6 September. On 7 September, the meridional gradient of \bar{T} from 60°S to 80°S becomes positive at 10 hPa (not shown), satisfying the definition for an SSW onset. On 2 September, a westward wind region appears above the strong westerly jet near $z = \sim 60$ km. The westward wind region remains until 22 September, descending to $z = \sim 40$ km but not reaching the 10-hPa level. Therefore, this event did not satisfy the criteria for a major SSW.

An eastward wind maximum above $z = \sim 80$ km is seen after 7 September. It is interesting that the eastward winds oscillate with a wave period of approximately 4–5 days in these regions. Note that this oscillation is also present in JAGUAR-DAS, which has no discrepancy in the time direction. Furthermore, the maximum of T occurs in the height region of $z = 80$ – 90 km after 20 September. Such a characteristic temperature structure is regarded as an MIL. Okui et al. (2021) reported the zonally asymmetric structure of the MIL that appeared during the SSW event in the Northern Hemisphere in the winter of 2018/2019. We confirmed that the MIL in SSW-SH 2019 also had a longitudinally dependent structure (not shown).

The wave forcing and residual mean circulation are included in the transformed Eulerian-mean (TEM) zonal momentum equation based on the primitive equation system as follows:

$$\bar{u}_t + \bar{v}^* \left[(a \cos \phi)^{-1} (u \cos \phi)_\phi - f \right] + \bar{w}^* \bar{u}_z = (\rho_o a \cos \phi)^{-1} \nabla \cdot \mathbf{F}, \quad (3-1)$$

$$\mathbf{F} \equiv \rho_o a \cos \phi \left(0, \bar{u}_z \frac{\bar{v}'\theta'}{\theta_z} - \bar{u}'v', \left[f - (\rho_o a \cos \phi)^{-1} (u \cos \phi)_\phi \right] \frac{\bar{v}'\theta'}{\theta_z} - \bar{u}'w' \right), \quad (3-2)$$

$$(\bar{v}^*, \bar{w}^*) \equiv \left(\bar{v} - \rho_o^{-1} \left(\rho_o \frac{\bar{v}'\theta'}{\theta_z} \right)_z, \bar{w} + (a \cos \phi)^{-1} \left(\cos \phi \frac{\bar{v}'\theta'}{\theta_z} \right)_\phi \right), \quad (3-3)$$

where a is the radius of the Earth, θ is the potential temperature, f is the

Coriolis parameter, ρ_o is the air density, and \mathbf{F} is the Eliassen-Palm (E-P) flux (Andrews et al., 1987).

Because of the downward control principle (Haynes et al., 1991), the negative wave forcings in the height region of $z = 30\text{--}80$ km drives poleward \bar{v}^* over $50\text{--}70^\circ\text{S}$ in the same height region (Figure 2c) and downward \bar{w}^* over the Antarctic region of $70\text{--}90^\circ\text{S}$ in the height region of $z = 20\text{--}70$ km (Figure 2d). The downward \bar{w}^* resulted in a temperature increase via adiabatic heating (Figure 2b). The wave forcings, that is the divergences of the E-P fluxes (EPFDs), are dominated by RWs in the height region of $z = 30\text{--}80$ km and by GWs in the height region of $z > 50$ km. In particular, the $s = 1$ RW EPFD largely contributes to the negative RW forcing in the height region of $z = 30\text{--}80$ km (Figure 2h). The dominance of the $s = 1$ RW corresponds to the fact that SSW-SH 2019 was a displacement-type SSW ($s = 1$).

Negative GW forcing is dominant in the height region of $z > 80$ km before 7 September, while the GW forcing is mostly positive and weakly oscillates with wave periods of $\sim 5\text{--}7$ days above $z \sim 60$ km after 7 September. Oscillations with wave periods of $\sim 5\text{--}7$ days are also seen in the $s = 1$ RW EPFD in the height region of $z > 60$ km after 10 September (Figure 2h). These characteristics are examined in more detail in Section 4.

3 Gravity Waves

In this section, we examine the time evolution of the horizontal distribution of GWs in the stratosphere and the MLT region. Figure 3 shows polar stereographic projection maps of $\overline{u'w'}$ associated with the GWs and GPH at heights of $z = 25, 40, 60, 75,$ and 90 km for the time periods of 25–27 August, 31 August–2 September, 6–8 September, 12–14 September, 18–20 September, and 24–26 September.

In the stratosphere (i.e., $z = 25$ km and 40 km), strongly negative $\overline{u'w'}$ is distributed along the polar vortex roughly centered at the South Pole before the SSW onset on 7 September. During the period of 6–8 September, including the SSW onset, the polar vortex shifts to the Western Hemisphere together with the strongly negative $\overline{u'w'}$ around the polar vortex edge. During the periods of 12–14 and 18–20 September, the polar vortex area becomes smaller and shifts further to lower latitudes of the Western Hemisphere. Strongly negative $\overline{u'w'}$ is observed at the edge of the polar vortex, particularly leeward of the South Andes and along the Antarctic coast. During the period of 24–26 September, the center of the polar vortex returns to the South Pole. The size of the polar vortex is smaller, and its edge is located south of 60°S . The negative $\overline{u'w'}$ weakens over the South Andes and becomes dominant leeward of the Ross Sea.

In the mesosphere (i.e., $z = 60$ km and 75 km), a strong polar vortex is clearly observed and largely negative $\overline{u'w'}$ is dominant around the polar vortex before the SSW onset. During the period of 6–8 September, the weakened vortex shifts primarily to the Western Hemisphere and largely positive $\overline{u'w'}$ is observed

around 50–60°S in the Eastern Hemisphere and at higher latitudes in the Western Hemisphere where the westward wind is dominant. At $z = 75$ km, the polar vortex is weakened and $\overline{u'w'}$ is largely positive at high latitudes and negative at low latitudes. During the period of 12–14 September, at $z = 60$ km, the polar vortex nearly disappears and positive $\overline{u'w'}$ appears around 50–60°S in the Eastern Hemisphere while but is significantly weakened at higher latitudes in the Western Hemisphere. At $z = 75$ km, the polar vortex becomes stronger, shifting its center slightly toward the Eastern Hemisphere, and weakly negative $\overline{u'w'}$ is dominant at low latitudes. During the period of 18–20 and 24–26 September, the polar vortex at $z = 60$ km gradually becomes stronger and the region with negative $\overline{u'w'}$ becomes dominant. At $z = 75$ km, the polar vortex becomes stronger and strongly negative $\overline{u'w'}$ is observed on the lower latitude side of the polar vortex. At $z = 90$ km, largely negative $\overline{u'w'}$ is dominant except during the periods of 6–8 September and 24–26 September; however, its distribution is complicated compared with that observed in lower height regions.

Figures 4a and 4b show time-height sections of $\overline{u'w'}$ and $\rho^{-1} \frac{d(\overline{\rho u'w'})}{dz}$, respectively, averaged over 50–70°S. The quantities in this figure are multiplied by $\rho^{\frac{1}{8}}$ in the vertical direction to make the structure easier to see. In all height regions, $\overline{u'w'}$ is largely negative before 2 September. When height regions with westward winds appear afterward, $\overline{u'w'}$ becomes slightly positive in the height region of $z > 60$ km. The height region with positive $\overline{u'w'}$ descends with the westward wind region after 9 September, while negative $\overline{u'w'}$ is observed above $z = \sim 70$ km. After 24 September, weakly positive $\overline{u'w'}$ appears again above $z = \sim 80$ km. For $\rho^{-1} \frac{d(\overline{\rho u'w'})}{dz}$ which corresponds to GW forcing, strongly negative values are dominant before 2 September for the height region of $z = 40$ –65 km. After 2 September, positive values are observed on and slightly above the positive $\overline{u'w'}$ regions.

Figures 4e and 4f show time-latitude sections of $\overline{\rho u'w'}$ and $\rho^{-1} \frac{d(\overline{\rho u'w'})}{dz}$, respectively, at $z = 40$ km, while Figures 4c and 4d show the same quantities at $z = 70$ km. At $z = 40$ km, largely negative $\overline{u'w'}$ is observed over 40–70°S in late August. The magnitude of the negative $\overline{u'w'}$ gradually decreases and shifts to higher latitudes until 20 September. In late September, the magnitude of negative $\overline{u'w'}$ increases again near 75°S. The latitude ranges of 40–70°S and 70–80°S correspond to the regions where the Southern Andes and the Antarctic Peninsula are located and to the Ross Sea, respectively. For $\rho^{-1} \frac{d(\overline{\rho u'w'})}{dz}$, negative values are dominant south of 40°S during the displayed time period, except south of 70°S during the period of 28 August–5 September. Conversely, at $z = 70$ km, strongly negative $\overline{u'w'}$ values are dominant south of 20°S before 3 September. During the period of 3–12 September, negative $\overline{u'w'}$ values are restricted to near 30°S and slightly positive $\overline{u'w'}$ values are observed for 50–70°S.

For $\rho^{-1} \frac{d(\overline{\rho u' w'})}{dz}$, negative values are dominant south of 20°S before 3 September. During the period of 3–22 September, after the SSW onset, slightly positive values are found for 40–70°S, while negative values are observed between 10°S and 40°S. After 22 September, the positive $\rho^{-1} \frac{d(\overline{\rho u' w'})}{dz}$ values approach zero.

4 Quasi-6-Day Waves

During SSW-SH 2019, a periodic oscillation with a wave period of ~5–7 days is observed above $z = \sim 60$ km in the time-height sections of \overline{U} and the $s = 1$ RW EPFD (Figure 2a and 2h). Because the RW behavior is consistent between JAGUAR and JAGUAR-DAS, the analysis of this wave is primarily based on JAGUAR-DAS, which is continuous in time. Figure 5a shows a longitude-time section of the GPH of the RWs at 60°S and $z = 70$ km. The $s = 1$ structure is clear throughout the analysis period. The $s = 1$ RWs with eastward and westward phase velocities are dominant before and after September 10, respectively.

Figure 5b shows frequency power spectra of the GPH fluctuations of the $s = 1$ RWs at $z = 70$ km as a function of the wave period (τ) and latitude. Near 60°S, there are peaks in several wave period ranges, namely at $\tau = \sim 2.5\text{--}3$, $\sim 3\text{--}5$, and $\sim 5\text{--}7$ days for eastward phase velocities, and at $\tau = \sim 3\text{--}5$, $\sim 5\text{--}7$, and $\sim 9\text{--}12$ days for westward phase velocities. Only the peak at $\tau = \sim 5\text{--}7$ days for the westward phase velocity components spread into both hemispheres; the other peaks are confined mostly south of 50°S. For the eastward phase velocity range, the $\sim 5\text{--}7$ -day peak is isolated, even though its spectral density is not necessarily large compared with those of the other peaks. Given the spectral characteristics, we define the component having $s = 1$ and $\tau = \sim 3.5\text{--}7$ days as a Q6DW. The frequency range is chosen to be sufficiently wide to extract a Q6DW packet. The Q6DWs are analyzed separately for the eastward (Q6DW-E) and westward (Q6DW-W) phase velocity components.

Figure 6a shows a latitude-time section of the GPH amplitudes of Q6DW-E (red contours) and Q6DW-W (blue contours) for the time period from January 2015 to July 2020 using the JAGUAR-DAS analysis data. Q6DW-E is amplified poleward of latitude of 40° every winter and spring in both hemispheres. Conversely, the year-to-year variation is large for the Q6DW-W amplitude. In years when strong Q6DW-W appear in boreal spring in 2015, in 2018, and in the austral spring of 2019 (i.e., SSW-SH 2019), Q6DW-W amplifies almost simultaneously in the mid- and high-latitudes of both hemispheres when Q6DW-E begins to decay in the winter and spring. The simultaneous amplification of Q6DW-W in both hemispheres is particularly evident during SSW-SH 2019. The amplitude of Q6DW-W in 2019 is slightly stronger and latitudinally broader in the Southern Hemisphere. Note that the amplitude of Q6DW-E in the Southern Hemisphere in 2019 is not particularly large compared with those of the other years.

Figure 6b shows latitude-time section of the GPH amplitudes of Q6DW-E and Q6DW-W for the time period from 22 August 2019 to 27 September 2019 at

$z = 70$ km according to the JAGUAR-DAS analysis data. Q6DW-E appears south of 40°S around 28 August and decays around 10 September. Conversely, the Q6DW-W amplitude is not very large until 10 September except from 30 August to 4 September in the range of $40\text{--}60^\circ\text{S}$ and from 4–11 September south of 70°S . Q6DW-W becomes dominant after 11 September in both hemispheres with its maximum near latitudes of 45° .

Figures 7a and 7b show the longitude-latitude and longitude-height cross sections, respectively, of the GPH component of Q6DW-E on 7 September, while Figures 7c and 7d show the same cross sections for Q6DW-W on 22 September. The Q6DW-E GPH amplitude is large only south of 40°S (Figure 7a). Its phases tilt eastward with height above $z = \sim 50$ km and westward below $z = \sim 50$ km, with the amplitude maximum observed at $z = \sim 65$ km (Figure 7b). Conversely, the Q6DW-W GPH component is symmetrically distributed with respect to the equator and is largest around latitudes of 40° in both hemispheres (Figure 7c). This horizontal distribution is similar to that of the normal-mode 5-day wave (e.g., Hirota et al., 1983). However, the longitude-height cross section of the Q6DW-W GPH component in Figure 7d shows that Q6DW-W is not barotropic like the normal mode. Q6DW-W has a significant phase tilt that is westward with height above $z = \sim 50$ km. Therefore, it is thought that Q6DW-W is not due to the normal mode. The Q6DW-W amplitude is larger at higher altitudes below $z = 90$ km.

Next, we examine excitation mechanisms of Q6DW-E and Q6DW-W. Figure 8a shows latitude-height cross section of the E-P fluxes and EPFD associated with Q6DW-E for the time period of 1–5 September 2019 according to the JAGUAR-DAS reanalysis data. During this period, Q6DW-E is active at high latitudes of the Southern Hemisphere (Figure 6b). The E-P fluxes in these figures are multiplied by $\rho^{\frac{1}{3}}$ in the vertical direction to make the structure easier to see. The EPFD is strongly positive in the height region of $z = 53\text{--}80$ km and negative in the height region of $30\text{--}53$ km south of 50°S . Strong downward E-P fluxes and relatively strong upward E-P fluxes are also observed south of 50°S in the height regions of $z = 50\text{--}70$ km and $z = 30\text{--}50$ km, respectively.

Figures 9a–c show latitude-height cross sections of the modified potential vorticity (MPV), given by the Ertel potential vorticity weighted by $\theta^{\frac{-5}{2}}$ (Lait, 1994) and meridional gradient of MPV ($\frac{d\text{MPV}}{dy}$), the static stability (N^2) and T , and the relative vorticity (ζ) and U , respectively, during the time period of 27–31 August according to the JAGUAR-DAS reanalysis data. This time period corresponds to 4 days before Q6DW-E becomes dominant (Figure 8a). Thus, there may be a characteristic feature related to the generation mechanism of Q6DW-E in this time period. There are a negative $\frac{d\text{MPV}}{dy}$ region extending from $z = \sim 90$ km at the South Pole to $z = \sim 60$ km at 40°S and a positive $\frac{d\text{MPV}}{dy}$ region below $z = 50$ km extending south of 40°S . The pair of positive and negative $\frac{d\text{MPV}}{dy}$ regions and the downward E-P flux on the boundary of the two regions are indicative of a baroclinic instability, even though the pattern is upside down with respect to that for a typical baroclinic instability in the troposphere. Note

that the positive and negative $\frac{dMPV}{dy}$ regions correspond well to the negative and positive EPFD regions observed south of 40°S where Q6DW-E is dominant.

The negative $\frac{dMPV}{dy}$ in the high-latitude mesosphere is due to the MPV minimum located at a slightly lower latitude (Figure 9a). Because MPV is proportional to $(f+\zeta)\cdot N^2$ (Lait, 1994), this MPV minimum corresponds to the broad maximum of N^2 and the negative maximum of ζ observed in Figure 9b and 9c, respectively. In the height range of $z = 65\text{--}75$ km, it is not the negative maximum of ζ but the maximum of N^2 that likely contributes to the formation of the MPV minimum. Conversely, in the height range of $z = 75\text{--}90$ km, the negative maximum of ζ corresponds to the MPV minimum.

Figures 10b and 10c show the latitude-height cross sections of the E-P fluxes and the EPFD associated with RWs and GWs, respectively, and Figure 10a shows the same quantities for the sum of the RWs and GWs (hereafter referred to as RWs+GWs), which were obtained from the high-resolution JAGUAR simulation for the time period of 22–26 August. This time period corresponds to 4 days before the broad N^2 maximum appears at a height of $z = \sim 70$ km for 50–70°S as shown in Figure 9b. The E-P fluxes in these figures are multiplied by $\rho^{\frac{1}{8}}$ in the vertical direction to make the structure easier to see. At $z = \sim 60$ km, the westerly jet splits into low and high latitudes and the GW forcing is larger at the top of each jet and at the lower height region between the two jets. The broad N^2 maximum is likely formed by the downward residual circulation (\bar{w}^*) driven by the negative GW forcing in the upper part of the jet on the lower latitude side. The negative forcing in this region is also caused by RWs, even though its structure is not as simple as that of GWs.

Next, we examine the spatial structure and excitation mechanism of Q6DW-W. Figure 8b and 8c show latitude-height cross sections of the E-P fluxes and the EPFD associated with Q6DW-W during the periods of 17–21 September and 11–15 September when Q6DW-W is mature and in the developing phase, respectively. During the period of 17–21 September, upward E-P fluxes are distributed in both hemispheres nearly symmetrically around the equator, even though the spread to higher latitudes is relatively small in the Northern Hemisphere. Negative EPFD values are observed near the latitude region of 20–80° above $z = \sim 80$ km in both hemispheres. The upward E-P fluxes in the Southern and Northern hemispheres appear from the height region of $z = 40\text{--}60$ km in 40–80°S and $z = 60\text{--}80$ km in 60–80°N, respectively, corresponding to the region where weakly positive EPFDs are distributed. During the period of 11–15 September in Figure 8c when Q6DW-W is its developing phase (Figure 6b), the upward E-P fluxes in the Southern Hemisphere change their direction from upward to northward, cross the equator, and reach the Northern Hemisphere above $z = \sim 80$ km.

Figures 9d, 9e, and 9f show latitude-height cross sections of the occurrence frequency of $\frac{dMPV}{dy} < 0$ and MPV, N^2 and T , and ζ and U , respectively, in the time period of 12–16 September corresponding to the developing phase of

Q6DW-W and 4 days before the Q6DW-W amplitude is maximized in both hemispheres. Around the regions with slightly positive EPFD in the height region of $z = 40\text{--}60$ km over $40\text{--}60^\circ\text{S}$ and $z = 60\text{--}80$ km south of 60°S (Figure 8b), the occurrence frequency of $\frac{d\text{MPV}}{dy} < 0$ reaches 40%–60% in the Southern Hemisphere and exceeds 80% in the Northern Hemisphere. Note that the existence of regions with $\frac{d\text{MPV}}{dy} < 0$ is a necessary condition of barotropic/baroclinic instability. These results suggest that Q6DW-W is an internal RW generated by the barotropic/baroclinic instability.

The region with $\frac{d\text{MPV}}{dy} < 0$ in the Northern Hemisphere can be found in the climatology (not shown). It is shown that GW forcing primarily contributes to the formation of the MPV maximum having a region with $\frac{d\text{MPV}}{dy} < 0$ on the higher latitude side (Sato et al., 2018). Conversely, the region with a relatively high occurrence of $\frac{d\text{MPV}}{dy} < 0$ in the Southern Hemisphere appears to be associated with the local minimum of MPV, which is located at relatively lower height regions of $z = 40\text{--}50$ km over $40\text{--}70^\circ\text{S}$ than the region where the GW forcing is dominant. This MPV local minimum is mainly attributed to the broad N^2 maximum observed around the same region in Figure 9e because there is no significant ζ minimum in Figure 9f.

Figures 10d–f show the latitude-height cross sections of the E-P fluxes and EPFD resulting from the RWs+GWs, RWs, and GWs, respectively, according to the high-resolution JAGUAR simulations during the time period of 7–11 September, respectively. This time period corresponds to 4 days before the broad N^2 maximum responsible for the negative $\frac{d\text{MPV}}{dy}$ is observed (Figure 9e). The EPFD of the RWs+GWs is largely positive in the triangular region from the height region of $z = 50\text{--}80$ km at 80°S to $z = \sim 70$ km at 40°S (Figure 10d) and is largely negative in the region spreading from the height region of $z = 20\text{--}50$ km at 80°S to $z = 20\text{--}70$ km at 40°S . A pair of positive and negative wave forcings is also observed north of 30°N at $z = 70\text{--}90$ km. These positive and negative EPFD pairs provide downward \bar{w}^* resulting in adiabatic heating (not shown). This adiabatic heating provides a positive T anomaly and causes the N^2 maximum below the anomaly.

In the Southern Hemisphere, EPFDs associated with RWs (Figure 10e) and GWs (Figure 10f) also correspond to a pair of positive and negative EPFD in nearly the same regions described for Figure 10d. For RWs, the positive EPFD in the triangular region is associated with Q6DW-E, as also seen in Figure 8a. Even though the time period of 7–11 September is 6 days after the dominant period of Q6DW-E (Figure 8a), Q6DW-E still has a large amplitude at high latitudes in the Southern Hemisphere (Figure 6b). The negative EPFD in the spreading region below $z = 50$ km over $40\text{--}80^\circ\text{S}$ is due to combination of the Q6DW-E (Figure 8a) and the RWs propagating from the troposphere. In addition, positive and negative EPFD resulting from GWs are observed above and below $z = 65$ km near $45\text{--}70^\circ\text{S}$. It is important that such a characteristic distribution of EPFD is due to GWs, i.e., GW forcing is related to the significant deceleration of the westerly polar night jet in the upper stratosphere and the

appearance of a weak easterly jet in the lower mesosphere, both of which are associated with SSW-SH 2019 (Figure 4). The GW forcing is slightly weaker than, but comparable to, the magnitude of the RW forcing, which indicates that both GWs and RWs contribute to the dynamically unstable field generating the strong Q6DW-W. This mechanism likely explains why the strong Q6DW-W is generated in association with the SSW event.

5 Summary and Concluding Remarks

We investigated the dynamical characteristics of the GWs and RWs during the SSW-SH 2019 event. Simultaneous observations by the PANSY radar and radiosondes were performed to examine the wind and temperature disturbances in the lower stratosphere associated with SSW-SH 2019. GW-permitting high-resolution JAGUAR simulations from the surface to the MLT region were conducted to examine the spatial distribution of the GWs and RWs, especially the Q6DWs and their contribution to the momentum budget.

First, we confirmed that high-resolution JAGUAR simulations can reproduce the appearance and distribution of wave-like disturbances, including GWs in the lower stratosphere, that are consistent with the PANSY radar and radiosonde observations. However, the magnitude of the GW momentum fluxes from the high-resolution JAGUAR simulations are approximately one-fifth of those observed by the PANSY radar. This may be due to the insufficient model resolution, particularly with respect to the steep terrain structure used in the high-resolution JAGUAR simulations.

Next, the time evolution of the GW momentum fluxes over the entire middle atmosphere was examined. Before the SSW onset, the zonal-mean $\overline{u'w'}$ associated with GWs was largely negative in almost all height regions for 50–70°S as usual. As the westward wind region appeared in association with the SSW onset, $\overline{u'w'}$ became weakly positive in the height region of $z > 60$ km. Not only the zonal-mean but also the horizontal distribution of the positive $\overline{u'w'}$ accorded well with the easterly wind region. Corresponding to this temporal evolution of $\overline{u'w'}$, the GW forcing, that is, the vertical convergence of $\overline{u'w'}$, was positive in the mesosphere and negative in the stratosphere for 50–70°S over the 20 days of 3–22 September after the SSW onset (Figure 4).

The spatial structures and excitation mechanism of the Q6DWs that were dominant during the SSW-SH 2019 event were also examined. The Q6DWs were composed of eastward (Q6DW-E) and westward (Q6DW-W) phase velocity components. Q6DW-E was dominant south of 40°S before 10 September, while Q6DW-W was dominant in both hemispheres and had its GPH maxima at ~40°S and ~40°N after 10 September. The phase of the GPH component of Q6DW-E tilted eastward with height above $z = \sim 50$ km, whereas that of Q6DW-W tilted westward with height above $z = \sim 60$ km, indicating that both Q6DW-E and Q6DW-W were not due to normal-mode 5-day RWs which should have barotropic structure.

It was shown that, while the appearance of Q6DW-E is common, the dominance of Q6DW-W appears to be unique to the SSW-SH 2019 event and that there is an SSW-specific Q6DW-W excitation mechanism. The excitation mechanism of the Q6DWs is schematically shown in Figure 11. Q6DW-E is thought to be an unstable wave from baroclinic instability and is characterized as a pair of negative and positive MPV meridional gradients in the vertical direction located in the mesosphere and the stratosphere, respectively, south of 40°S (Figure 11b). This inference is supported by the fact that the region with $\frac{dMPV}{dy} < 0$ in the mesosphere disappeared when Q6DW-E was no longer observed (not shown). The MPV minimum resulting in $\frac{dMPV}{dy} < 0$ in the mesosphere was maintained by the N^2 maximum and the ζ minimum. In the height range of $z = 65\text{--}75$ km, not ζ but rather N^2 primarily contributed to the formation of the MPV minimum. Conversely, in the height range of $z = 75\text{--}90$ km, the negative maximum of ζ corresponds to the MPV minimum (Figure 11b). The ζ minimum corresponded to the westerly jet tilted poleward with height in the mesosphere. The negative GW and RW forcings, which extended over $z = 70\text{--}80$ km at 25–40°S played an essential role in forming the N^2 maximum (Figure 11a). Note that this MPV time evolution is unusual.

The Q6DW-W was likely an internal RW generated by the barotropic/baroclinic instability in the height region of $z = 40\text{--}60$ km over 60–80°S. This dynamic instability was characterized as the MPV minimum at 40–70°S and $z = 40\text{--}50$ km (Figure 11d) and corresponds to the broad N^2 maximum in the same region. This N^2 maximum was likely caused by a downward residual flow from $z = \sim 50$ km at 80°S to $z = \sim 60$ km at 40°S (Figure 11c). This downward residual circulation was driven by the RW and GW forcing. The RW forcing was due to the Q6DW-E and RWs propagating from the mid- and high-latitude troposphere. The GW forcing, which was important and unique to the SSW event, played a significant role: positive GW forcing occurred in the mesosphere where the polar vortex largely shifted and weakened because of the SSW and negative GW forcing occurred in the stratosphere where the polar night jet was still maintained (Figure 4).

These excitation mechanisms of Q6DW-E and Q6DW-W are consistent with the appearance of Q6DW-E every winter in both hemispheres at high latitudes, whereas Q6DW-W extending over both hemispheres was unusually observed in September 2019 when an SSW occurred in the Southern Hemisphere (Figure 6a). The positive GW forcing in the mesosphere associated with the shifted polar vortex during the SSW is a unique feature of the September 2019 event. However, note that the strong SSW was not the only reason for the Q6DW-W dominance in both hemispheres because such a Q6DW-W was not clearly observed in February 2018 or January 2019, when strong SSW events occurred in the Northern Hemisphere. Consequently, mechanisms other than the occurrence of an SSW event may be required for the generation of Q6DW-W.

GW forcing plays an important role in the excitation mechanism of both Q6DW-E and Q6DW-W. However, note that the comparison with the PANSY radar

observations indicated a large underestimation ($\sim 1/5$) in the model-simulated momentum fluxes associated with GWs, even though the location and structure of the simulated GWs were realistic. Thus, in the real atmosphere, the role of GW forcing in Q6DW excitation could be much more important than that shown in this study using the model. Although the GW forcing was estimated to be weaker than the RW forcing, it may be as large as, or even larger than, the RW forcing.

It was also shown that the E-P fluxes associated with Q6DW-W crossed the equator above $z = \sim 80$ km during the period of 10–15 September when Q6DW-W began to appear in the Southern Hemisphere. This result indicates several possible mechanisms for the spread of Q6DW-W. Q6DW-W can spread directly from the Southern Hemisphere to the Northern Hemisphere. Furthermore, the Q6DW-W propagating from the Southern Hemisphere may excite RWs in the Northern Hemisphere in regions where the necessary condition of dynamical instability is satisfied ($\frac{dMPV}{dy} < 0$). However, it is unclear whether this mechanism can explain the phase synchronization of the Q6DW-W in the Northern and Southern hemispheres (Figure 7c).

In future work, it will be necessary to examine the interannual variation of Q6DWs in terms of EPFDs caused by GWs and RWs, including RWs originating from the troposphere and the Q6DW-E. What determines the time lag between the appearance of the barotropic/baroclinic instability and the onset of Q6DW-W is also an important subject for future study.

Acknowledgments

This study is supported by JST CREST grant JPMJCR1663, JSPS KAKENHI grants 201703536, and the Integrated Research Program for Advancing Climate Models (TOUGOU) Grant No. JPMXD0717935715 from the Ministry of Education, Culture, Sports, Science and Technology (MEXT), Japan. PANSY is a multi-institutional project with core members from The University of Tokyo, the National Institute of Polar Research, and the Kyoto University. The PANSY radar and radiosonde measurements at Syowa Station are operated by the Japanese Antarctic Research Expedition (JARE). Operational radiosonde observation data at Syowa Station is provided by the Japan Meteorological Agency (JMA). The hindcasts by JAGUAR were performed using the Earth Simulator at the Japan Agency for Marine-Earth Science and Technology (JAMSTEC). All figures except citations were created using the Dennou Club Library (DCL). We are grateful to Dai Koshin for the numerical simulations on JAGUAR-DAS. Finally, we would like to appreciate the members of the 60th Japanese Antarctic Research Expedition (JARE60) for their enormous support of our observations at Syowa Station.

Open Research

The PANSY radar observational data are available at the project website: <http://pansy.eps.s.u-tokyo.ac.jp>. All the raw data, metadata, and saved session files necessary for re-producing the figures in this paper are available

at <https://doi.org/10.5281/zenodo.5793119>. For legal reasons, the source code for the GCM cannot be publicly released. It has been (will be) made available to the editor and reviewers, and is available to anyone who contacts the corresponding author.

Figure 1. Time-height sections of (a) zonal winds (u), (b) vertical winds (w), and (c) zonal momentum vertical fluxes ($\overline{\rho u' w'}$) (color) and the background zonal wind (\overline{U}) (contour) observed by the Program of the Antarctic Syowa (PANSY) radar and (d) temperature (T) observed by the radiosondes. The panels on the right half show time-height sections of (e) u , (f) w , (g) $\overline{\rho u' w'}$ and \overline{U} , and (h) T from the high-resolution Japanese Atmospheric General circulation model for Upper Atmosphere Research (JAGUAR) simulations. Black triangles show the tropopause height observed by the radiosondes. The contour intervals are 10 m s^{-1} , 10 m s^{-1} , and 10 K for u , \overline{U} , and T , respectively. In panels (e)–(h), the boundary of each run is shown by solid black lines.

Figure 2. Time-height sections of (a) the background zonal wind (\overline{U}) meridionally averaged over $50\text{--}70^\circ\text{S}$, (b) the background temperature (\overline{T}) meridionally averaged over $70\text{--}90^\circ\text{S}$, and (c) the meridional ($\overline{v^*}$) and (d) vertical ($\overline{w^*}$) component of the residual mean circulation averaged over $50\text{--}70^\circ\text{S}$ and $70\text{--}90^\circ\text{S}$, respectively, according to the high-resolution JAGUAR simulations. Time-height sections of Eliassen-Palm flux divergences (EPFD) for (e) Rossby waves (RWs)+gravity waves (GWs), (f) RWs, (g) GWs, and (h) the $s = 1$ RW according to the high-resolution JAGUAR simulations. For panels (e)–(h), \overline{U} is overlaid as contours with an interval of 10 m s^{-1} .

Figure 3. Polar-stereographic projections of $\overline{u' w'}$ (color) and the geopotential height (GPH) (contours) according to the high-resolution JAGUAR simulation at $z = 25, 40, 60, 75,$ and 90 km for 25–27 August, 31 August–2 September, 6–8 September, 12–14 September, 18–20 September, and 24–26 September. The contour intervals are 400 m for $z = 25 \text{ km}$ and 40 km , 200 m for $z = 60 \text{ km}$ and 75 km , and 100 m for $z = 90 \text{ km}$. The cyan dots indicate the location of Syowa Station.

Figure 4. Time-height sections of (a) $\overline{u' w'}$ (color) and (b) $\rho^{-1} \frac{d(\overline{\rho u' w'})}{dz}$ meridionally averaged over $50\text{--}70^\circ\text{S}$. The values are multiplied by $\rho^{0.25}$ in the vertical direction. Time-latitude sections of $\overline{\rho u' w'}$ and $\rho^{-1} \frac{d(\overline{\rho u' w'})}{dz}$ at (e and f) $z = 40 \text{ km}$ and (c and d) 70 km are also shown. For these panels, \overline{U} is overlaid as contours with an interval of 10 m s^{-1} .

Figure 5. (a) Longitude-time section of the GPH of RWs in the height region of $z = 70 \text{ km}$ and 60°S . (b) Wave period (τ) and latitude section of the frequency power spectra of the GPH ($\omega P_Z(k = 1, \omega, y)$) at $z = 70 \text{ km}$ shown as the energy content description for August and September 2019.

Figure 6. Latitude-time sections of the amplitude of GPH associated with quasi-6-day waves (Q6DWs) with westward phase velocity (Q6DW-W) (blue)

and eastward phase velocity (Q6DW-E) (red) at $z = 70$ km (a) from January 2015 to July 2020 and (b) from 22 August to 27 September 2019. The contour intervals are 50 m.

Figure 7. Longitude-latitude cross sections of the GPH of (a) Q6DW-E and (c) Q6DW-W with a contour interval of 50 m. Longitude-height cross sections of GPH of (b) Q6DW-W and (d) Q6DW-W with a contour interval of 60 m are also shown. Data in JAGUAR-Data Assimilation System (JAGUAR-DAS) on 7 September and 22 September are used for Q6DW-E and Q6DW-W, respectively.

Figure 8. Latitude-height cross sections of the E-P flux (vector) and EPFD (color) of (a) Q6DW-E during the period of 1–5 September, (b) Q6DW-W during the period of 17–21 September, and (c) Q6DW-W during the period of 11–15 September from JAGUAR-DAS. In these panels, \bar{U} is overlaid as contours with an interval of 10 m s^{-1} .

Figure 9. Latitude-height cross sections of (a) the modified potential vorticity (MPV) (contour) with a contour interval of 3 PVU and the meridional gradient of MPV ($\frac{d\text{MPV}}{dy}$) (color), (b) the static stability (N^2) (color) and T (contour) with a contour interval of 10 K, and (c) the vorticity (ζ) (color) and \bar{U} (contour) with a contour interval of 10 m s^{-1} during the period of 27–31 August. Latitude-height cross sections of (d) the occurrence frequency of $\frac{d\text{MPV}}{dy} < 0$ [%] (color) and MPV (contour) with a contour interval of 3 PVU, (e) N^2 (color) and T (contour) with a contour interval of 10 K, and (f) ζ (color) and \bar{U} (contour) with a contour interval of 10 m s^{-1} during the period of 12–16 September.

Figure 10. Latitude-height cross sections of the E-P flux (vector) and EPFD (color) of (a) RWs+GWs, (b) RWs, and (c) GWs during the period of 22–26 August and (d) RWs+GWs, (e) RWs, and (f) GWs during the period of 7–11 September. \bar{U} is overlaid as contours with an interval of 10 m s^{-1} .

Figure 11. Schematic illustration of (a) the wave forcing and residual mean circulation for the period of 22–26 August 2019 and (b) excitation mechanisms of Q6DW-E for the period of 27–31 August 2019. The same but for Q6DW-W are shown in panel (c) for 12–16 September 2019, and panel (d) for 7–11 September 2019.

References

- Andrews, D. G., Holton, J. R., & Leovy, C. B. (1987). *Middle atmosphere dynamics No. 40*. Academic press.
- Butler, A. H., Seidel, D. J., Hardiman, S. C., Butchart, N., Birner, T., & Match, A. (2015). Defining Sudden Stratospheric Warmings. *Bulletin of the American Meteorological Society*, 96(11), 1913–1928. <https://doi.org/10.1175/BAMS-D-13-00173.1>
- Haynes, P. H., McIntyre, M. E., Shepherd, T. G., Marks, C. J., & Shine, K. P. (1991). On the “Downward Control” of Extratropical Diabatic Circulations by Eddy-Induced Mean Zonal Forces. *Journal of Atmospheric Sciences*, 48(4), 651–678. [https://doi.org/10.1175/1520-0469\(1991\)048<0651:OTCOED>2.0.CO;2](https://doi.org/10.1175/1520-0469(1991)048<0651:OTCOED>2.0.CO;2)
- Hirota, I., Hirooka, T., & Shiotani,

M. (1983). Upper stratospheric circulations in the two hemispheres observed by satellites. *Quarterly Journal of the Royal Meteorological Society*, 109(461), 443–454. <https://doi.org/10.1002/QJ.49710946102>Kodera, K. (2006). Influence of stratospheric sudden warming on the equatorial troposphere. *Geophysical Research Letters*, 33(6). <https://doi.org/10.1029/2005GL024510>Kohma, M., & Sato, K. (2014). Variability of upper tropospheric clouds in the polar region during stratospheric sudden warmings. *Journal of Geophysical Research: Atmospheres*, 119(17), 10,100–10,113. <https://doi.org/10.1002/2014JD021746>Koshin, D., Sato, K., Miyazaki, K., & Watanabe, S. (2020). An ensemble Kalman filter data assimilation system for the whole neutral atmosphere. *Geoscientific Model Development*, 13(7), 3145–3177. <https://doi.org/10.5194/GMD-13-3145-2020>Koshin, D., Sato, K., Kohma, M., & Watanabe, S. (2021). An update on the 4D-LETKF data assimilation system for the whole neutral atmosphere. *Geoscientific Model Development Discussions*, 1–25. <https://doi.org/10.5194/GMD-2020-381>Lait, L. R. (1994). An Alternative Form for Potential Vorticity. *Journal of Atmospheric Sciences*, 51(12), 1754–1759. [https://doi.org/10.1175/1520-0469\(1994\)051<1754:AAFFPV>2.0.CO;2](https://doi.org/10.1175/1520-0469(1994)051<1754:AAFFPV>2.0.CO;2)Lieberman, R. S., Riggins, D. M., Franke, S. J., Manson, A. H., Meek, C., Nakamura, T., ... Reid, I. M. (2003). The 6.5-day wave in the mesosphere and lower thermosphere: Evidence for baroclinic/barotropic instability. *Journal of Geophysical Research: Atmospheres*, 108(D20), 4640. <https://doi.org/10.1029/2002JD003349>Lim, E. P., Hendon, H. H., Butler, A. H., Garreaud, R. D., Polichtchouk, I., Shepherd, T. G., ... Newman, P. A. (2020). The 2019 Antarctic sudden stratospheric warming. *SPARC Newsletter*, 54, 10–13.Limpasuvan, V., Orsolini, Y. J., Chandran, A., Garcia, R. R., & Smith, A. K. (2016). On the composite response of the MLT to major sudden stratospheric warming events with elevated stratopause. *Journal of Geophysical Research: Atmospheres*, 121(9), 4518–4537. <https://doi.org/10.1002/2015JD024401>Liu, H. L., Talaat, E. R., Roble, R. G., Lieberman, R. S., Riggins, D. M., & Yee, J. H. (2004). The 6.5-day wave and its seasonal variability in the middle and upper atmosphere. *Journal of Geophysical Research: Atmospheres*, 109(D21), 21112. <https://doi.org/10.1029/2004JD004795>Manney, G. L., Schwartz, M. J., Krüger, K., Santee, M. L., Pawson, S., Lee, J. N., ... Livesey, N. J. (2009). Aura Microwave Limb Sounder observations of dynamics and transport during the record-breaking 2009 Arctic stratospheric major warming. *Geophysical Research Letters*, 36(12). <https://doi.org/10.1029/2009GL038586>Matsuno, T. (1971). A Dynamical Model of the Stratospheric Sudden Warming. *Journal of Atmospheric Sciences*, 28(8), 1479–1494. [https://doi.org/10.1175/1520-0469\(1971\)028<1479:ADMOTS>2.0.CO;2](https://doi.org/10.1175/1520-0469(1971)028<1479:ADMOTS>2.0.CO;2)Meyer, C. K., & Forbes, J. M. (1997). A 6.5-day westward propagating planetary wave: Origin and characteristics. *Journal of Geophysical Research: Atmospheres*, 102(D22), 26173–26178. <https://doi.org/10.1029/97JD01464>Minamihara, Y., Sato, K., Tsutsumi, M., & Sato, T. (2018). Statistical Characteristics of Gravity Waves With Near-Inertial Frequencies in the Antarctic Troposphere and Lower Stratosphere Observed by the PANSY Radar. *Journal of Geophysical Research: Atmospheres*, 123(17), 8993–9010. <https://doi.org/10.1029/2017JD028128>Minamihara, Y.,

Sato, K., & Tsutsumi, M. (2020). Intermittency of Gravity Waves in the Antarctic Troposphere and Lower Stratosphere Revealed by the PANSY Radar Observation. *Journal of Geophysical Research: Atmospheres*, *125*(15), e2020JD032543. <https://doi.org/10.1029/2020JD032543>

Okui, H., Sato, K., Koshin, D., & Watanabe, S. (2021). Formation of a Mesospheric Inversion Layer and the Subsequent Elevated Stratopause Associated With the Major Stratospheric Sudden Warming in 2018/19. *Journal of Geophysical Research: Atmospheres*, *126*(18). <https://doi.org/10.1029/2021JD034681>

Reichler, T., Kim, J., Manzini, E., & Kröger, J. (2012). A stratospheric connection to Atlantic climate variability. *Nature Geoscience* *2012* *5*:11, *5*(11), 783–787. <https://doi.org/10.1038/ngeo1586>

Sato, K., O’Sullivan, D. J., & Dunkerton, T. J. (1997). Low-frequency inertia-gravity waves in the stratosphere revealed by three-week continuous observation with the MU radar. *Geophysical Research Letters*, *24*(14), 1739–1742. <https://doi.org/10.1029/97GL01759>

Sato, K., Yasui, R., & Miyoshi, Y. (2018). The Momentum Budget in the Stratosphere, Mesosphere, and Lower Thermosphere. Part I: Contributions of Different Wave Types and In Situ Generation of Rossby Waves. *Journal of the Atmospheric Sciences*, *75*(10), 3613–3633. <https://doi.org/10.1175/JAS-D-17-0336.1>

Sato, K., & Nomoto, M. (2015). Gravity Wave-Induced Anomalous Potential Vorticity Gradient Generating Planetary Waves in the Winter Mesosphere. *Journal of the Atmospheric Sciences*, *72*(9), 3609–3624. <https://doi.org/10.1175/JAS-D-15-0046.1>

Sato, K., Tsutsumi, M., Sato, T., Nakamura, T., Saito, A., Tomikawa, Y., ... Yamanouchi, T. (2014). Program of the Antarctic Syowa MST/IS radar (PANSY). *Journal of Atmospheric and Solar-Terrestrial Physics*, *118*, 2–15. <https://doi.org/10.1016/J.JASTP.2013.08.022>

Schoeberl, M. R., & Hartmann, D. L. (1991). The Dynamics of the Stratospheric Polar Vortex and Its Relation to Springtime Ozone Depletions. *Science*, *251*(4989), 46–52. <https://doi.org/10.1126/science.251.4989.46>

Talaat, E. R., Yee, J. H., & Zhu, X. (2002). The 6.5-day wave in the tropical stratosphere and mesosphere. *Journal of Geophysical Research: Atmospheres*, *107*(D12), ACL 1-1. <https://doi.org/10.1029/2001JD000822>

Tomikawa, Y., Nomoto, M., Miura, H., Tsutsumi, M., Nishimura, K., Nakamura, T., ... Sato, K. (2015). Vertical Wind Disturbances during a Strong Wind Event Observed by the PANSY Radar at Syowa Station, Antarctica. *Monthly Weather Review*, *143*(5), 1804–1821. <https://doi.org/10.1175/MWR-D-14-00289.1>

Tomikawa, Y., Sato, K., Watanabe, S., Kawatani, Y., Miyazaki, K., & Takahashi, M. (2012). Growth of planetary waves and the formation of an elevated stratopause after a major stratospheric sudden warming in a T213L256 GCM. *Journal of Geophysical Research: Atmospheres*, *117*(D16), 16101. <https://doi.org/10.1029/2011JD017243>

Watanabe, S., & Miyahara, S. (2009). Quantification of the gravity wave forcing of the migrating diurnal tide in a gravity wave-resolving general circulation model. *Journal of Geophysical Research: Atmospheres*, *114*(D7), 7110. <https://doi.org/10.1029/2008JD011218>

Watanabe, S., Kawatani, Y., Tomikawa, Y., Miyazaki, K., Takahashi, M., & Sato, K. (2008). General aspects of a T213L256 middle atmosphere general circulation model. *Journal of Geophysical Research: Atmospheres*, *113*(D12), 12110.

<https://doi.org/10.1029/2008JD010026>Watanabe, S., Tomikawa, Y., Sato, K., Kawatani, Y., Miyazaki, K., & Takahashi, M. (2009). Simulation of the eastward 4-day wave in the Antarctic winter mesosphere using a gravity wave resolving general circulation model. *Journal of Geophysical Research: Atmospheres*, *114*(D16), 16111. <https://doi.org/10.1029/2008JD011636>Wu, D. L., Hays, P. B., & Skinner, W. R. (1994). Observations of the 5-day wave in the mesosphere and lower thermosphere. *Geophysical Research Letters*, *21*(24), 2733–2736. <https://doi.org/10.1029/94GL02660>Yamazaki, Y., Matthias, V., Miyoshi, Y., Stolle, C., Siddiqui, T., Kervalishvili, G., ... Alken, P. (2020). September 2019 Antarctic Sudden Stratospheric Warming: Quasi-6-Day Wave Burst and Ionospheric Effects. *Geophysical Research Letters*, *47*(1), e2019GL086577. <https://doi.org/10.1029/2019GL086577>Yasui, R., Sato, K., & Miyoshi, Y. (2018). The Momentum Budget in the Stratosphere, Mesosphere, and Lower Thermosphere. Part II: The In Situ Generation of Gravity Waves. *Journal of the Atmospheric Sciences*, *75*(10), 3635–3651. <https://doi.org/10.1175/JAS-D-17-0337.1>Yasui, R., Sato, K., & Miyoshi, Y. (2021). Roles of Rossby Waves, Rossby–Gravity Waves, and Gravity Waves Generated in the Middle Atmosphere for Interhemispheric Coupling. *Journal of the Atmospheric Sciences*, *78*(12), 3867–3888. <https://doi.org/10.1175/JAS-D-21-0045.1>